A Retrofit 60 Hz Current Sensor for Non-Intrusive Power Monitoring at the Circuit Breaker

Zachary Clifford *Member, IEEE*, John J. Cooley *Student Member, IEEE*, Al-Thaddeus Avestruz *Member, IEEE*,
Zack Remscrim, Dan Vickery, and Steven B. Leeb *Fellow, IEEE*

Abstract—We present a new sensor for power monitoring that measures current flow in a circuit breaker without permanent modification of the breaker panel or the circuit breaker itself. The sensor consists of three parts: an inductive pickup for sensing current from the breaker face, an inductive link designed to transmit power through the steel breaker panel door, and a passive, balanced JFET modulator circuit for transmitting information through the inductive link. The demodulated breaker current signal is available outside of the breaker panel door. This sensor provides a solution for low-cost, non-intrusive retrofit of any circuit breaker panel for centralized power monitoring.

Index Terms—Home power monitoring, non-intrusive load monitoring, load diagnostics, circuit breaker

I. INTRODUCTION AND MOTIVATION

Non-Intrusive Load Monitoring (NILM) is an approach to electrical system diagnostics and power monitoring that has a potentially much lower sensor count than other load-specific monitoring systems. A NILM identifies and monitors individual loads on a power distribution system by measuring the frequency content of transient events in the current signals from a centralized location. Work with this technology was demonstrated in [1]–[12].

The current signal for the NILM is typically measured using a magnetic field sensor wrapped around the utility feed for the circuit to be monitored. Such a sensor may be impractical for some retrofit applications, especially in the home where skilled labor would be required to separate line and neutral in order to deploy a wrap-around magnetic field sensor, or in industrial environments where electrical service cannot be interrupted. The sensor presented in this paper is an alternative to the wrap-around magnetic field sensor. It measures the current in the utility feed by sensing the magnetic field at the face of any circuit breaker in a standard breaker panel, where the line and neutral are already separated. A major challenge, overcome by the system presented here, is communicating through the steel breaker panel door, which typically must be closed to comply with safety regulations.

II. SYSTEM OVERVIEW

The sensor shown in Figure 1(a) consists of three parts: an inductive pickup for sensing current from the breaker face (Breaker Pickup), an inductive link designed to transmit power through the steel breaker panel door (Through-door Inductive Link), and a balanced JFET modulator circuit for transmitting information through the inductive link (JFET Mixer).

The outer coil in Figure 1(a) is driven with a high-frequency sinusoidal carrier voltage. That voltage couples to the inner
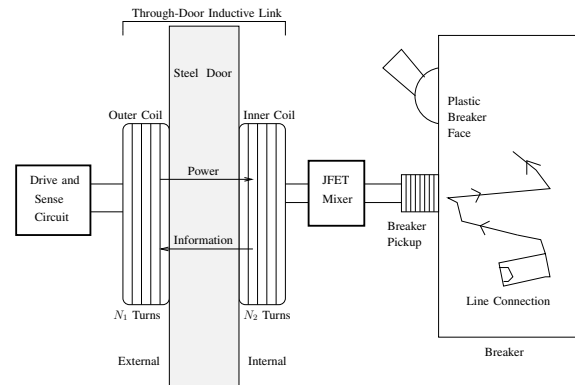
(a) Sensor block diagram

(b) Circuit Breaker Cross-section

Fig. 1. The current sensor measures magnetic fields at the face of the circuit breaker and modulates a high frequency carrier signal to transmit that information through the panel door.

coil through the inductive link and drives the JFET mixer. The JFET mixer controls the amount of current drawn from the inner coil according to the low-frequency (60 Hz) current signal measured by the breaker pickup. The result is a modulation between the high frequency carrier signal and the low-frequency (60 Hz) signal measured at the breaker face. The external sense circuit in Figure 1(a) monitors the current drawn through the inductive link to extract the resulting modulated signal. The JFET modulator is fully powered by the applied carrier, and the entire system works without modification to the breaker panel or the circuit breaker itself. With the modulated signal available to the sense circuit external to the door, the current through the main breaker may be analyzed with a

NILM or other power monitoring system for load identification and diagnostics.

III. BREAKER PICKUP

This section describes the inductive sensor referred to as the "breaker pickup" in Figure 1(a). The current path inside a typical circuit breaker passes by the lower face as suggested by Figures 1(a) and 1(b). The breaker pickup, positioned outside the breaker on its lower face, was designed to focus and measure the magnetic field resulting from current flowing inside the breaker.
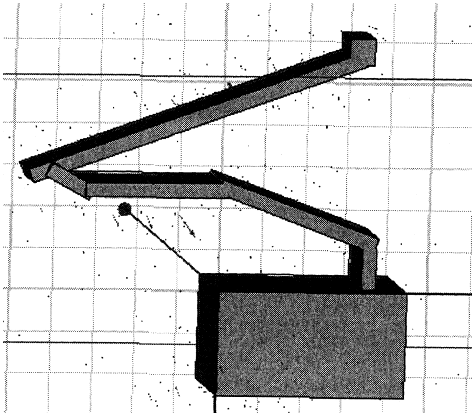

Fig. 2.   Maxwell 3D model of the circuit breaker

Ansoft's Maxwell 3D was used to model the magnetic fields generated by the current-carrying member inside a typical circuit breaker. The geometric model of the current-carrying member shown in Figure 2 was developed to match the geometry common to several brands of circuit breakers. The simulated magnetic fields were used to identify the appropriate location of the breaker pickup. Various breaker pickup shapes were considered to yield sufficient concentration of magnetic flux in the pickup core. Simulations using the finite element modeling software, FEMM, verified that a half toroid of high permeability material placed on the breaker face was suitable. A typical FEMM simulation is depicted in Figure 3.
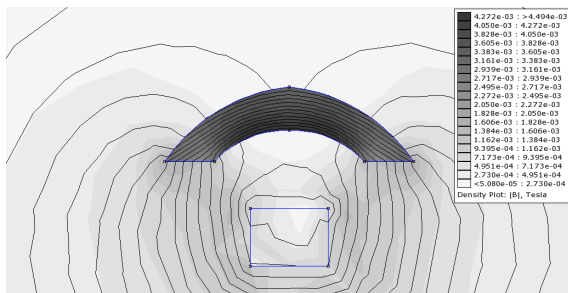

Fig. 3.   Finite Element Magnetic Model (FEMM) of magnetic flux through the breaker. The plastic breaker is ignored because it is neither conductive nor affected by the magnetic field.
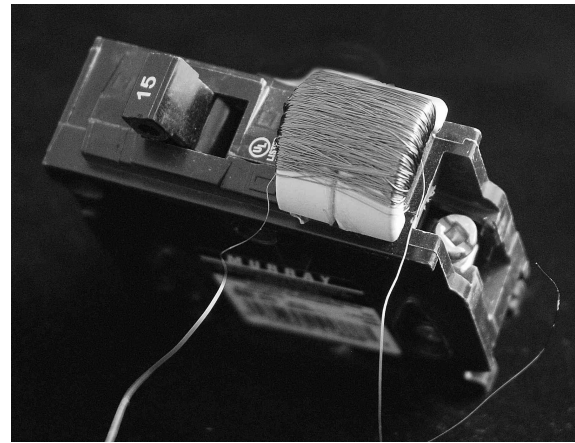

Fig. 4.   Breaker pickup photograph.

To form the magnetic yoke, a core[1] with relative permeability of 10,000 was first cut in half. The two halves were then joined for increased cross-sectional area. A total of 1,200 turns of 34 AWG magnet wire were wrapped around the yoke. A photograph of the breaker pickup affixed to the breaker face is shown in Figure 4. Maximizing the number of turns, cross-sectional area and relative permeability was important for increasing the inductance of the breaker pickup. The resulting inductive impedance at 60 Hz was sufficient to provide suitable voltage signals corresponding to the breaker current.

IV. JFET MIXER

The four-quadrant balanced JFET modulator (mixer), shown in Figure 5, was designed to transmit information from the breaker pickup through the inductive link and out of the breaker panel. This circuit consists of two JFET devices for modulation control and two resistors to improve linearity, but it does not require a DC power supply.
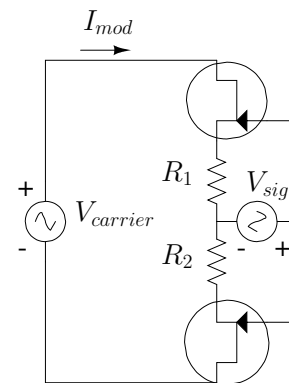

Fig. 5.   Adaptive Referencing Balanced two-JFET Modulator circuit enables simultaneous powering and modulation with no DC bus.

The JFET mixer can be modeled as a time-varying load on the carrier voltage source, $V_{carrier}$ in Figure 5, that

[1]Ferroxcube TX25/15/10-3E6 [13]

445

corresponds to the voltage on the inner coil in Figure 1(a). The load presented to $V_{carrier}$ in Figure 5 varies with the control signal, V_{sig}, applied to the JFET gates and leads to a corresponding modulation of the current I_{mod}. The two-JFET mixer circuit is particularly advantageous for this application because it requires a minimal amount of circuitry inside the breaker door and lends itself to a low-cost solution.

The JFET is a normally-on device that requires a negative gate-to-source voltage, V_{gs}, to turn it off. It may be modeled as a symmetric device, so that the drain and source are interchangeable and determined by which leg of the JFET has the lower potential. On positive half cycles ($V_{carrier} > 0$), the source of each device is the lower leg and the drain, the upper leg. The gate-source voltage of the lower device is the positive-valued drain-source voltage of the lower device added to the positive-valued drop across R_2 and V_{sig}. If the 60 Hz signal, V_{sig}, is sufficiently small, the lower device maintains a strictly positive gate-source voltage for most of the positive half cycle of the carrier signal. Thus the lower device can be taken to be fully on during that time, well-modeled by a small resistance. Meanwhile, the upper device has a gate-to-source voltage that is V_{sig} minus the positive drop across R_1. Again, if the 60Hz signal, V_{sig}, is sufficiently small, the upper device maintains a gate-source voltage that may not be strictly positive so that, instead of behaving as a small resistor, it is controlled so that its current varies according to the 60 Hz signal measured at the breaker face. In general, the gate-source voltage for the lower device contains a positive dc offset compared to that of the upper device even if they are not strictly positive and strictly negative respectively.

The roles of the two devices reverse when the polarity of the carrier signal reverses. The result is a modulation of the carrier signal current by the 60 Hz signal. The JFET mixer is adaptively-referencing because during both positive and negative half-cycles of $V_{carrier}$, one device is fully-on, referencing the source of the other device to low-potential end of the mixer circuit.

The behavior described above can be validated by simulations (LTSPICE) of the circuit in Figure 5. Figure 6(a) shows simulations of the gate-to-source voltages for the upper and lower devices with for a fixed positive carrier voltage. The gate-to-source voltage of the lower device is more positive than that of the upper device. Figure 6(b) shows the resulting 60Hz-modulated current when the circuit is excited with an ac-carrier voltage of 5kHz. Note that the quantities in the simulations of Figure 6 were chosen to provide illustrative visualizations of the behavior but do not necessarily correspond to design values or signal levels in our experimental setup. The plots of Figure 6 are also identical upon reversing the JFET devices with respect to the drain and source terminals, consistent with the drain-source symmetry of the JFETs described above.

The experimental setup is built with PN4117A JFET devices from Fairchild semiconductor, and 1.2 kΩ resistors to improve linearity. Modulation behavior was confirmed experimentally.
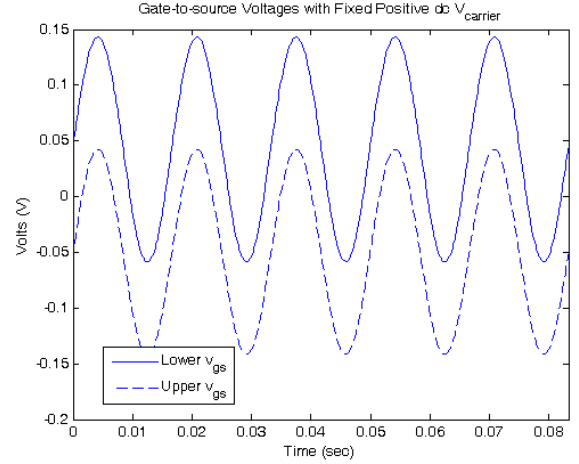
(a) Gate-to-source voltages with a fixed dc $V_{carrier} = 10V$.
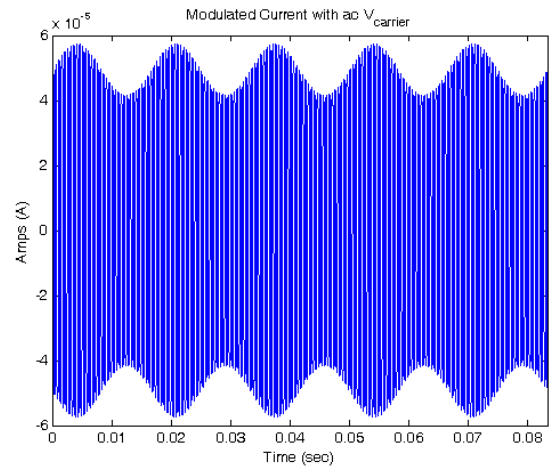
(b) Modulated current, I_{mod}, with a 2kHz 10V amplitude $V_{carrier}$.

Fig. 6. Balanced JFET Mixer, adaptive referencing and modulation behavior. PN4117 devices, $R_1 = R_2 = 1k\Omega$, $|V_{sig}| = 0.1$V, $f_{sig} = 60$Hz.

V. THROUGH-DOOR INDUCTIVE LINK

The inductive link across the steel door shown in Figure 1(a) consists of two resonant coils wrapped around samarium cobalt magnets with a N_1:N_2 turns ratio. These two coils and the steel door form a magnetic circuit linking the two coils. We take the magnetic reluctance model of Figure 7 to model the behavior of the inductive link. Reluctance is given in Equation (1) where l is the magnetic path length and A is the magnetic area.

$$R = \frac{l}{\mu A} \tag{1}$$

The MMF generators $N_1 I_p$ and $N_2 I_2$ model the effect of the two coils and the reluctances capture the magnetic paths in the pieces of the physical system. Most notably, the reluctance of the path through the steel door, R_{steel}, is generally small because of the high permeability of steel. This presents a design challenge for the inductive link because R_{steel} tends

to shunt magnetic flux away from the desired magnetic path. That is, the steel door acts as a shield to the magnetic fields. The inductive link was designed to overcome the challenge
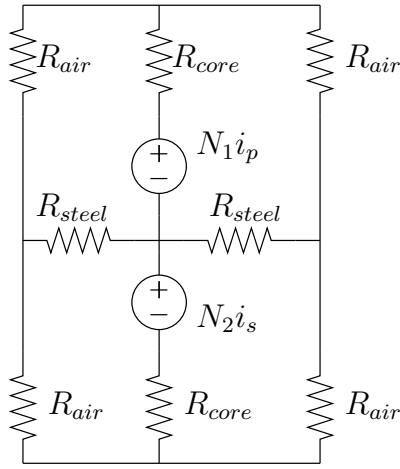

Fig. 7.   Reluctance model of through door transmission

Fig. 8.   Top view of transmission coil configuration

described above by selecting (empirically) an optimum carrier frequency. At high frequency, the permeability of the steel diminishes thereby decreasing the shielding effect due to the ferromagnetism in the steel [14]. However, at high frequency, the shielding effect due to eddy currents induced in the steel intensifies. Therefore, we expect an optimum frequency where the shielding due to high-frequency eddy currents and low-frequency magnetic permeability is minimized. We attempt, in our experimental setup, to further reduce the permeability of the steel using strong magnets. The arrangement of the magnets (Figure 8) is intended to saturate the magnetic domains in the steel thereby increasing the reluctance R_{steel} in the model of Figure 7. Moreover, the magnets provide a convenient means of securing the device to the door. Finally, the coil geometry itself is broad and flat yielding a large A and a small l for the reluctance described in equation (1).

The signal of interest to the sense circuitry of Figure 1(a) is the current drawn by the JFET mixer on the inside of the door. That current is the high-frequency carrier modulated with the low-frequency (60 Hz) signal sensed from the breaker face. A large turns ratio, $\frac{N_2}{N_1}$, yields a large voltage gain to the inner coil to develop the necessary drain-source voltages in the JFET mixer. Also, a large turns ratio amplifies the current drawn by the JFET mixer to the outer coil. The number of turns on the inner coil may consist of as many turns of wire as allowed by the physical space, while the number of turns on the outer coil is lower-bounded by the current drive capability of the power source driving it.

A useful carrier frequency for the through-door inductive link was found empirically as follows. The demodulated 60Hz signal output was viewed on an oscilloscope while the carrier frequency was adjusted. For each adjustment of the carrier frequency, the capacitance comprising the sense impedance Z_{sense} was adjusted to maximize the demodulated signal at
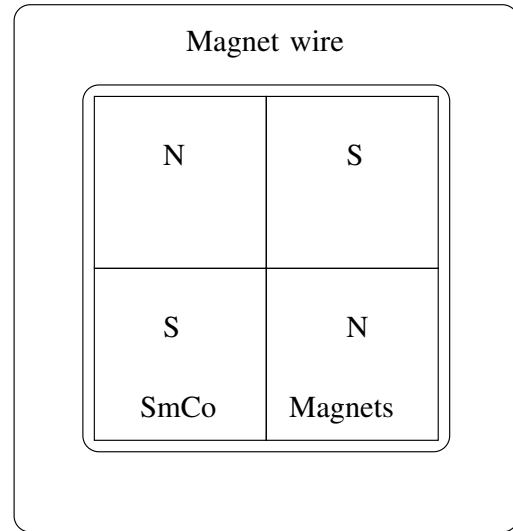
that frequency. A suitable carrier frequency of approximately 220kHz was identified for our experimental setup. This method of carrier frequency selection can be automated if the carrier frequency and primary side current sense impedance are electronically adjustable.

VI.   SENSE AND DEMODULATION CIRCUIT

The sense circuit is a DSP-based I/Q demodulation circuit. It consists of a power front-end responsible for driving the outer coil, an analog signal chain for demodulating the signal, and a DSP for performing post processing.

A. Power front-end

The power front-end, shown in Figure 9, is a push-pull driver composed of two BJT devices. The bases of these BJT devices are driven using a high voltage decompensated operational amplifier in a high gain configuration. A square wave at the carrier frequency is ac-coupled to the noninverting input of the amplifier. The operational amplifier then increases the voltage to a level suitable for driving the push-pull driver.
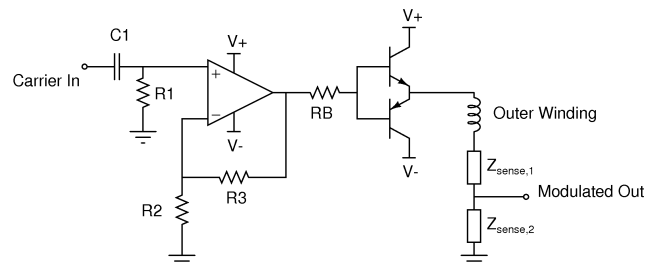

Fig. 9.   A simplified schematic of the coil drive power front-end.

The push-pull driver is connected to the series combination of the outer coil and two sense impedances. The voltage between the two sense impedances is taken as the input to

the analog filter chain. The total sense impedance is matched to the coil impedance at the carrier frequency, but the ratio of the two impedances is chosen to deliver acceptable voltage levels to the analog signal chain.

B. Signal Processing and I/Q Demodulation

A block diagram of the analog signal chain is shown in Figure 10. The analog front end measures the voltage across the coil sense impedance, V_{sense}. In-phase and quadrature reference signals multiply the measured signal resulting in the I and Q channels shown. Multiplication is achieved with a full-bridge consisting of analog switches. The demodulated signal is followed by a low-pass filter that attenuates the remaining high frequency content. While the signal of interest is demodulated to 60 Hz, the unsuppressed carrier in the input signal is demodulated to dc. Removing the resulting dc offset with a highpass filter allows for a large gain before sampling. A final low-pass filter reduces aliasing in the sampled signal, while an offset of 1.65 V centers the signal in the input voltage range of the 12-bit ADC[2]. The I and Q channels are combined using a dsPIC33 to form the final output signal. Here, we discuss some tradeoffs in various implementations of I/Q demodulation while highlighting the method used in our experimental setup.

An amplitude modulated signal with unsuppressed-carrier content can be represented by

$$
\begin{aligned}
R(t) = &\, A \cos\left(\omega_c t + \phi\right) \\
&+ \frac{M}{2} \left(\cos\left((\omega_c + \omega_m)t + \phi\right) + \cos\left((\omega_c - \omega_m)t + \phi\right)\right),
\end{aligned}
$$
(2)

where ω_c is the carrier frequency, A is the unsuppressed carrier amplitude, $M/2$ is the amplitude of the modulated signal, ω_m is the modulation frequency, and ϕ is a phase offset. The system presented here is inherently an unsuppressed carrier system because the parallel current path through the magnetizing inductance of the through door link will always yield a carrier signal in addition to the modulated signal. The phase term, ϕ, is unknown or time-varying because it depends on the properties of the breaker panel door in addition to the properties of the through door link and the modulator circuit. I/Q demodulation is used to detect the signal and cancel out the phase term.

To produce the I and the Q-channel signals, the received signal, represented by $R(t)$ above, is multiplied by in-phase and quadrature reference signals, represented by $\cos\left(\omega_c t\right)$ and $\sin\left(\omega_c t\right)$ in Figure 10. Assuming high frequency terms have been perfectly eliminated by the ensuing low-pass filter, the final signals can be shown to be

$$
I(t) = \cos\left(-\phi\right)\left(\frac{M}{2}\cos\omega_m t + \frac{A}{2}\right)
$$
(3)

$$
Q(t) = \sin\left(-\phi\right)\left(\frac{M}{2}\cos\omega_m t + \frac{A}{2}\right).
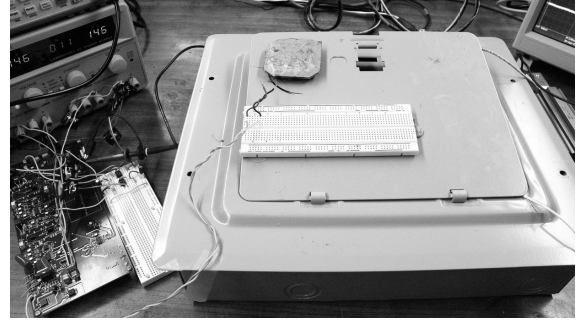$$
(4)

[2]Internal to the dsPIC33FJ256MC710

Fig. 11. Entire experimental setup with circuit breaker door closed. The outer through door coil and demodulation circuitry are visible.

The final step in I/Q demodulation would be to take the square root of the sum of the squares of $I(t)$ and $Q(t)$ in equations (3) and (4) above. The result of that operation would be the desired signal

$$
S(t) = \frac{M}{2}\cos\omega_m t + \frac{A}{2},
$$
(5)

in which the unknown phase terms have been eliminated by combining the I and Q signals.

In our experimental setup, the signals in (3) and (4) are first high-pass filtered to remove the $A/2$ offset terms before sampling. This allows for a significant gain (x100 in Figure 10) and an improvement in the SNR of the sampled signal. However, the filtered signal is bipolar and the ensuing sum of squares operation described above would normally be stripped of the original sign information. While, in principle, this sign information could be recovered from knowledge of ϕ, in practice, the value of ϕ is unknown and may drift in time. One approach is to add an offset to the signal after the HPF and gain. This removes sign ambiguity, but will also reduce the accuracy of the I/Q demodulation result because the added offset creates an unwanted nonlinearity in the sum of squares calculation. An alternate approach would be to retain the offset (remove the HPF in Figure 10). However, in that approach, the remaining dc offset will limit the ensuing gain. A compromise between these two extremes would be to only remove a fraction of the $\frac{A}{2}$ offset. If this fraction is properly selected, the remaining offset, $\frac{A'}{2}$, may remove the sign ambiguity while still allowing for a sufficient gain without saturation. This approach would effectively control the modulation depth of the sampled signal. In the current experimental setup, the sum of squares operation is performed after adding an artificial offset which yields the tradeoff between sign ambiguity and accuracy described above.

VII. EXPERIMENTAL SETUP AND RESULTS

A photograph of the experimental setup is shown in Figure 11. An HP 6834B ac power source was used to generate test current signals. The current pickup was secured to the breaker face with leads running to a circuit attached to the inside surface of the steel door. This was connected to the
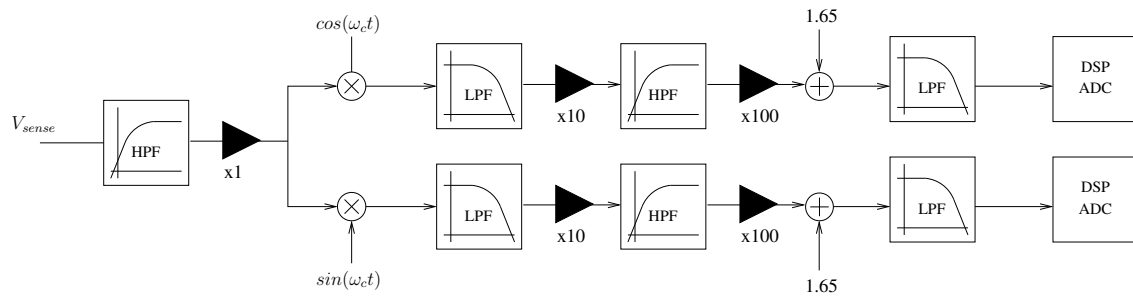
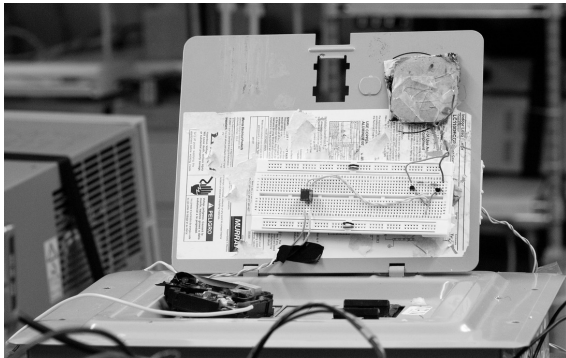Fig. 10. Block diagram of analog filter chain

Fig. 12. Experimental setup with circuit breaker door open. The JFET Mixer, test circuit breaker, and inner coil are visible.
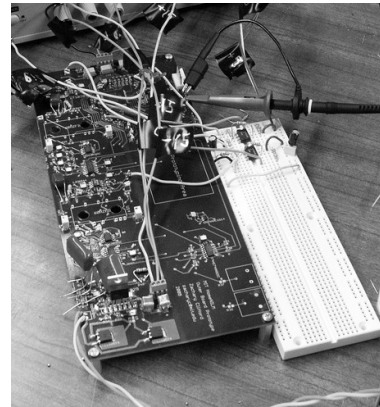

Fig. 13. Demodulation board attached to power supply.

14.4:1 step-up transformer, the Tamura MET-01, before being connected to the JFET modulator. This portion of the setup is shown in Figure 12. The JFET modulator was built on the same breadboard and connected to the inner coil.

The inner coil consisted of 1000 turns of 34 AWG magnet wire wrapped around four samarium cobalt magnets of dimension 1/2"x1/2"x1/4" and grade 26 MGOe arranged as shown in Figure 8. The outer coil was similarly constructed with a set of permanent magnets arranged so that the N and S poles of magnets on opposite sides of the door were facing each other. The outer coil was wound with 24 windings and then connected to the signal processing electronics described above.

Experimental results from the prototype monitoring hardware are shown in Figures 14 and 15. The HP 6834B ac source was used to provide different frequencies and amplitudes of current through the test circuit breaker monitored by the prototype sensor. The programmable ac source made it possible to control the current frequency, permitting not only 60 Hz sinusoidal currents, but also higher frequencies that might appear in distorted current waveforms with higher harmonic content, e.g., as might arise in the current drawn by an unfiltered or lightly filtered full-bridge rectifier at the front-end of a power supply.

Figure 14 shows the performance of the current sensor for two different frequencies of current, 60 Hz and 180 Hz, flowing through the breaker. The 180 Hz current represents third harmonic content, typical in current waveforms distorted by rectification. The two current waveforms, shown in Figure 14 in graphs (a) and (b), are shown during experiments with individual frequency currents for clarity, although the sensor works well for combined currents with fundamental 60 Hz content and harmonic distortion. The current levels in both tests correspond to 5 A peak.

The middle graphs in Figure 14, graphs (c) and (d), show spectrum analyzer plots of the modulated carrier on the primary side or "outside" the door of the circuit breaker panel. As expected, the spectrum shows a strong peak at the carrier frequency. The side-lobes correspond to the modulating current signal, at 60 Hz and 180 Hz differences from the carrier frequency.

The lower graphs in Figure 14, graphs (e) and (f), show the reconstructed or demodulated current signals on the primary side as computed by the DSP microcontroller. The amplitudes of the signals are scaled by the transfer characteristic pickup core at the face of the breaker. That is, the inductance of the pickup core varies with the frequency of the sensed magnetic field and associated current, filtering the lower frequencies in favor of the higher frequencies, as shown in Figure 14. This is a predictable variation with frequency, and can be easily "inverted" with a digital filter (not employed to make Figure 14) on the primary side in the DSP microcontroller "outside" of the breaker panel. That is, the final output of a full sensor

449

(a) 60 Hz sine wave input

(b) 180 Hz sine wave input

(c) 60 Hz sine wave magnitude at carrier frequency

(d) 180 Hz sine wave magnitude at carrier frequency

(e) 60 Hz sine wave demodulated output
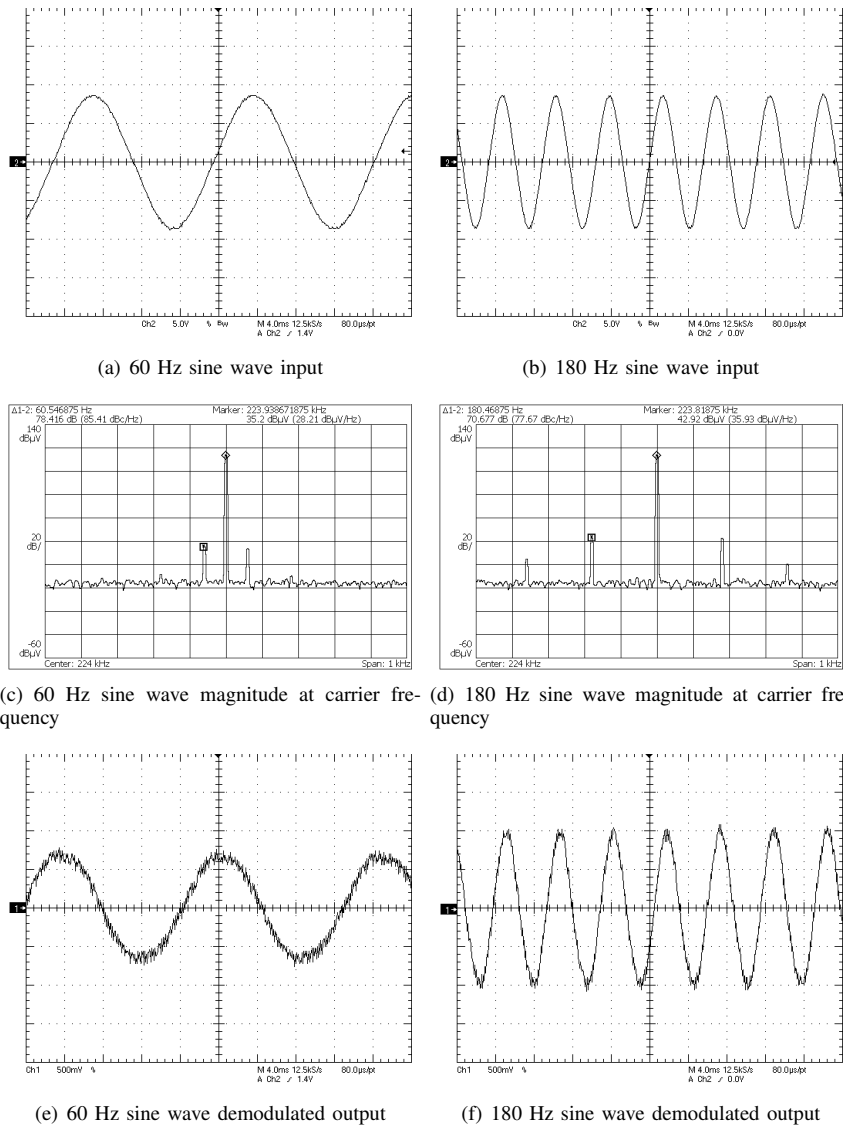

(f) 180 Hz sine wave demodulated output

Fig. 14. (a) and (b): Breaker currents generated for testing, (c) and (d): frequency spectrum of the signal received outside the door prior to demodulation, (e) and (f): demodulated signals corresponding to the breaker currents in (a) and (b).
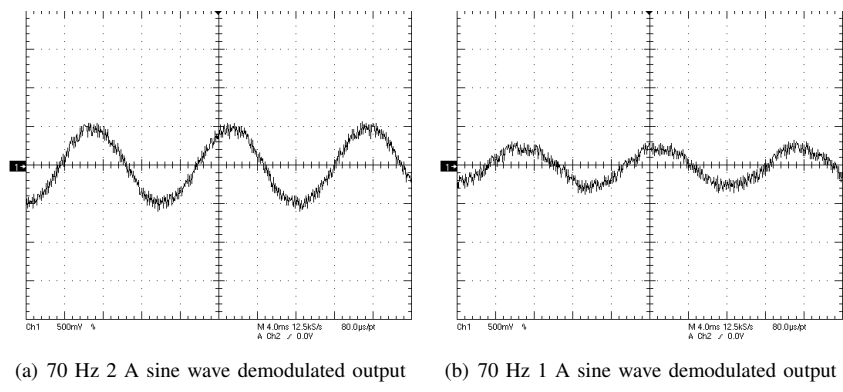

(a) 70 Hz 2 A sine wave demodulated output

(b) 70 Hz 1 A sine wave demodulated output

Fig. 15. 70 Hz test signals were generated to verify that measured signals were not simply 60 Hz ambient pickup.

450

system would be scaled in software with a digital filter to recover the correct current amplitudes.

Figure 15 shows demodulation and processing of a 70 Hz signal. The first graph (a) shows the output of the sensor when a 2A, 70 Hz current is passing through the breaker. The second graph (b) shows the output of the sensor for a 1A, 70 Hz current. This test demonstrates that the output of the sensor system is robust with respect to "pick-up". That is, this test indicates that the sensor is not corrupted by other 60 Hz signals in the general environment of the monitored breaker and circuit panel. Since 70 Hz is not among the harmonics of 60 Hz, this shows that the signal being measured is actually from the test current source and not unwanted pickup from the air.

The prototype sensor has successfully detected currents as small as 100 mA in amplitude, and should be able to detect substantially smaller currents with signal processing hardware optimized for low noise and higher digital resolution.

VIII. CONCLUSION

The U.S. Department of Energy has identified "sensing and measurement" as one of the "five fundamental technologies" essential for driving the creation of a "Smart Grid" [15]. Consumers will need "simple, accessible. . . , rich, useful information" to help manage their electrical consumption without interference in their lives [15]. Both vendors and consumers will likely find innumerable ways to mine information if it is made available in a useful form. However, appropriate sensing and information delivery systems remain a chief bottleneck for many applications, and metering hardware and access to metered information will likely limit the implementation of new electric energy conservation strategies in the near future.

Closed or "clamp" core sensors wrapped around the utility feed are often used to provide current sense signals to energy monitoring systems. These sensors prohibit widespread monitoring because skilled labor must separate line and neutral in order to deploy a wrap-around magnetic field sensor, even in the case of separable core sensors. This paper proposes an alternative to traditional clamp or Hall-effect sensors. This alternative requires no skilled installation. This sensor measures the current in the utility feed by sensing the resulting magnetic field at the face of the main (or other) circuit breaker in a standard breaker panel. The sensor can be interrogated through the steel panel door with no direct electrical contact, permitting the door to remain closed to comply with safety regulations.

The proposed sensor could be a "silver bullet" for many power monitoring and control problems. The sensor is as easy to install in a retrofit situation as in new work. This approach could make it easy to provide essential, comprehensible information about opportunities and the success of efforts for energy conservation.

Acknowledgments

REFERENCES

[1] J. S. Ramsey, S. B. Leeb, T. DeNucci, J. Paris, M. Obar, R. Cox, C. Laughman, and T. J. McCoy, "Shipboard applications of non-intrusive load monitoring," in *American Society of Naval Engineers Reconfigurability and Survivability Symposium*, Atlantic Beach, Florida, February 2005.

[2] T. DeNucci, R. Cox, S. B. Leeb, J. Paris, T. J. McCoy, C. Laughman, and W. Greene, "Diagnostic indicators for shipboard systems using non-intrusive load monitoring," in *IEEE Electric Ship Technologies Symposium*, Philadelphia, Pennsylvania, July 2005.

[3] W. Greene, J. S. Ramsey, S. B. Leeb, T. DeNucci, J. Paris, M. Obar, R. Cox, C. Laughman, and T. J. McCoy, "Non-intrusive monitoring for condition-based maintenance," in *American Society of Naval Engineers Reconfigurability and Survivability Symposium*, Atlantic Beach, Florida, February 2005.

[4] S. B. Leeb, S. R. Shaw, and J. J. L. Kirtley, "Transient event detection in spectral envelope estimates for nonintrusive load monitoring," *IEEE Transactions on Power Delivery*, vol. 10, no. 3, pp. 1200–1210, July 1995.

[5] L. K. Norford and S. B. Leeb, "Non-intrusive electrical load monitoring in commercial buildings based on steady state and transient load-detection algorithms," *Energy and Buildings*, vol. 24, pp. 51–64, 1996.

[6] U. A. Khan, S. B. Leeb, and M. C. Lee, "A multiprocessor for transient event detection," *IEEE Transactions on Power Delivery*, vol. 12, no. 1, pp. 51–60, 1997.

[7] S. R. Shaw, S. B. Leeb, L. K. Norford, and R. W. Cox, "Nonintrusive load monitoring and diagnostics in power systems," *IEEE Transactions on Instrumentation and Measurement*, vol. 57, no. 7, pp. 1445–1454, July 2008.

[8] G. R. Mitchell, R. W. Cox, J. Paris, and S. B. Leeb, "Shipboard fluid system diagnostic indicators using non-intrusive load," *Naval Engineers Journal*, vol. 119, no. 1, November 2007.

[9] J. P. Mosman, R. W. Cox, D. McKay, S. B. Leeb, and T. McCoy, "Diagnostic indicators for shipboard cycling systems using non-intrusive load monitoring," in *American Society for Naval Engineers Day 2006*, Arlington, VA, June 2006.

[10] R. W. Cox, P. Bennett, D. McKay, J. Paris, and S. B. Leeb, "Using the non-intrusive load monitor for shipboard supervisory control," in *IEEE Electric Ship Technologies Symposium*, Arlington, VA, May 2007.

[11] G. Mitchell, R. W. Cox, M. Piber, P. Bennett, J. Paris, W. Wichakool, and S. B. Leeb, "Shipboard fluid system diagnostic indicators using nonintrusive load monitoring," in *American Society for Naval Engineers Day 2007*, Arlington, VA, June 2007.

[12] E. Proper, R. W. Cox, S. B. Leeb, K. Douglas, J. Paris, W. Wichakool, L. Foulks, R. Jones, P. Branch, A. Fuller, J. Leghorn, and G. Elkins, "Field demonstration of a real-time non-intrusive monitoring system for condition-based maintenance," in *Electric Ship Design Symposium*, National Harbor, Maryland, February 2009.

[13] I. Ferroxcube, "Tx25/15/10-3e6 datasheet," Available http://www.ferroxcube.com/prod/assets/tx251510.pdf.

[14] N. Bowler, "Frequency-dependence of relative permeability in steel," *Review of Quantitative Nondestructive Evaluation*, vol. 25, pp. 1269–1276, 2006.

[15] U. S. D. of Energy, "The smart grid: An introduction," August 2009.